Geosci. Instrum. Method. Data Syst. Discuss., doi:10.5194/gi-2016-32, 2016
Manuscript under review for journal Geosci. Instrum. Method. Data Syst.
Published: 1 November 2016

Geoscientific Instrumentation Methods and Data Systems Discussions
Open Access
EGU

A joint thermal and electromagnetic diagnostics approach for the inspection of thick walls

Nicolas Le Touz[1,2], Jean Dumoulin[1,2], Gianluca Gennarelli[3], and Francesco Soldovieri[3]

[1]LUNAM university, IFSTTAR, COSYS-SII, F-44340, Bouguenais, France
[2]INRIA/IRISA, I4S Team, Campus de Beaulieu, 35042 Rennes, France
[3]CNR, IREA, 328 Via Diocleziano, 80124 Naples, Italy

Correspondence to: Nicolas Le Touz (nicolas.le-touz@ifsttar.fr)

Abstract. In this study, we present a numerical inversion approach to detect and localize inclusions in thick walls under natural solicitations. The approach is based on a preliminary analysis of the surface temperature field evolution with time (for instance acquired by infrared thermography); after, this analysis is improved by taking advantage of *a priori* information provided by ground penetrating radar reconstructions of the structure under investigation. In this way, it is possible to improve the accuracy of the images achievable with the stand-alone thermal reconstruction method in the case of quasi-periodic natural excitation.

1 Introduction

The issue of the integration of geophysical methods is a topic of timely interest and several fields can benefit of this strategy such as monitoring of the environment, infrastructure protection, cultural heritage management.

In this scientific frame, several efforts have been made and interesting results and strategies are drawn in (Eppelbaum, 2014; Alperovich et al., 2013)

Here we propose to combine two complementary approaches by coupling thermal and electromagnetic reconstructions both based on contact-less field measurements. The non-destructive diagnostic approach presented in this paper aims at detecting and localizing inclusions in thick walls by exploiting surface thermal and ground penetrating radar measurements. Here, we consider inclusions in the structure, which may represent for example delaminations or inner cavities, whose prompt identification is crucial in structural health monitoring applications.

The identification of thermal sources (heat flux) or thermal properties (thermal conductivity and/or capacity) of a material has numerous applications. Indeed, a variation of the thermal parameters may be the signature of an inclusion and the identification process is typically performed by solving an inverse thermal problem. Few reconstruction methods have been proposed to solve the inverse thermal problem, either for source reconstruction (Beck J.V., 1985) or parameters reconstruction (Ozisik, 2000). In both the cases, it is necessary to solve an optimization problem, involving the search of a global minimum of a cost function representing the difference between the collected measurements and the model data. Some optimization approaches based on conjugate gradient or Levenberg-Marquardt algorithm and using adjoint state method have been developed in one dimensional (Ozisik, 2000) or in multidimensional scenarios (Jarny et al., 1991).

Geosci. Instrum. Method. Data Syst. Discuss., doi:10.5194/gi-2016-32, 2016
Manuscript under review for journal Geosci. Instrum. Method. Data Syst.
Published: 1 November 2016

Geoscientific Instrumentation Methods and Data Systems Discussions
Open Access
EGU

In this frame, a method based on adjoint state and finite element method has been developed in recent years by IFSTTAR with the aim to reconstruct the thermal field over a given domain (Nassiopoulos, 2008; Crinière et al., 2014). Afterward, this method has been extended to the reconstruction of the thermal properties of thick walls in two dimensional (Brouns, 2014; Brouns et al., 2014) or three dimensional (Nassiopoulos and Bourquin, 2010) geometries. Nevertheless, the results obtained with this method suffer of the large variations of the retrieved parameters near the instrument boundaries because of side effects (Brouns et al., 2014).

In order to reduce these spurious effects, we propose in this work to use the thermal reconstruction method by gaining information by an electromagnetic diagnostics approach based on ground penetrating radar (GPR) surveys. To this end, the data are collected by a long term thermal monitoring with an adapted infrared thermography system in combination with a GPR.

As well-known, GPR imaging has proved to be useful in several application fields, e.g. the detection of buried pipes, landmines, defects in structures like bridges or roads, the investigation of archaeological sites, etc. (Persico, 2014).

The working principle of the GPR is the same of the traditional radar save for the fact that wave propagation occurs in a lossy dielectric medium instead of free-space. A wide-band electromagnetic pulse is radiated in the investigated medium and, owing to the presence of subsurface anomalies, a part of this wave is scattered/reflected and the backscattered signal is collected by a receiving antenna (Daniels, 2004). Therefore, as for the thermal imaging, GPR imaging relies upon the fact that the electromagnetic signal is capable to penetrate inside opaque materials. Starting from the knowledge of the scattered field, a reconstruction of the dielectric properties of the investigated scene can be achieved by solving an electromagnetic inverse scattering problem, which is is non-linear and ill-posed (Soldovieri et al., 2009).

The diagnostic approach proposed in this work couples both thermal and electromagnetic reconstruction methods and consists in three stages. First a preliminary thermal inversion is carried out to identify possible anomalies in the structure. After, a GPR reconstruction is performed to refine the preliminary and rough localization of potential inclusions acheved by the thermal method. Finally, the information about the scenario provided by GPR reconstructied image is exploited in the thermal inverse modeling to improve the accuracy of this method.

The paper is organized as follows. The thermal inverse model is detailed in Sec. 2. After, Sec.3 deals with the electromagnetic inverse scattering approach. Sec. 4 describes the way in which the "geometrical" information provided by GPR is exploited for the thermal data inversion. Numerical examples assessing the effectiveness of the proposed inversion approach are reported in Sec. 5. Conclusions and perspectives are addressed in Sec. 6.

2 Thermal modeling

The 2D geometry relevant to the thermal reconstruction problem is sketched in Fig.1. It is assumed that temperature measurements are collected at the upper surface of the investigated structure, which is a rectangular wall containing few anomalies. The acquisition of the surface temperature time-evolution can be carried out by infrared thermography coupled with environmental

Geosci. Instrum. Method. Data Syst. Discuss., doi:10.5194/gi-2016-32, 2016
Manuscript under review for journal Geosci. Instrum. Method. Data Syst.
Published: 1 November 2016

Geoscientific Instrumentation Methods and Data Systems Discussions
Open Access
EGU

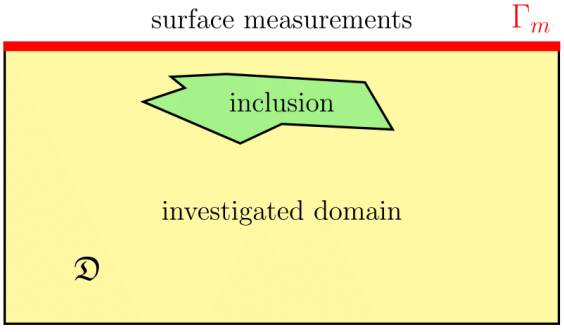

Figure 1. Geometry of the problem (MODIFY FIGURE ADDING AIR, WALL, AIR TO INDICATE THE THREE REGIONS. ADD ALSO Γ_0

sensors as presented in (Dumoulin et al., 2013; Dumoulin and Boucher, 2014). Such an outdoor experimental set-up permits to survey and record the pseudo-periodic evolution of the temperature for several days under natural solicitations.

A direct thermal model is first established to get numerical temperature data at the surface of the investigated wall. Then, a thermal inversion is performed with the adjoint state method in order to get the reconstruction of the shallower part of the investigated wall. The direct and inverse thermal models are described as follows.

2.1 Thermal state computation

As shown in Fig.1, the measurements are performed along the upper wall surface Γ_m. A heat flux, convective exchanges with the ambient air, and radiative exchanges with the sky arise at this surface. On the other wall surfaces Γ_0, an adiabatic constraint has been imposed.

The heat equation for the investigated wall $\mathfrak{D}$ is written as

$$\begin{cases} \rho c \frac{\partial T}{\partial t} - \nabla \cdot (k \nabla T) = 0 & \text{for } (x,t) \in \mathfrak{D} \times [0,t_a] \\ k \nabla T \cdot \boldsymbol{n} = \Phi_s + h\,(T_a(t) - T(x,t)) + h_{rad}\,(T_s(t) - T(x,t)) & \text{for } (x,t) \in \Gamma_m \times [0,t_a] \\ k \nabla T \cdot \boldsymbol{n} = 0 & \text{for } (x,t) \in \Gamma_0 - \times [0,t_a] \\ T(x,0) = T_0(x) & \text{for } x \in \mathfrak{D} \end{cases} \quad (1)$$

where $T(x,t)$ is the temperature at the generic location x for the time t, ρc is the thermal capacity, k is the thermal conductivity, ϕ is a thermal flux, h is the convective exchange coefficient, h_{rad} is the equivalent radiative exchange coefficient $h_{rad} = \varepsilon\sigma(T_{surf}+T_s)(T_{surf}^2+T_s^2)$ (temperatures here in K). This coefficient is obtained with the linearization of the Stefan's law. Moreover, ε is the emissivity of the surface, σ is Stefan's constant, T_{surf} is the temperature at the surface, T_s is the sky temperature, T_a is the air temperature $\boldsymbol{n}$ is the outward-pointing normal, Γ_m is the boundary located at the surface of the domain, where measurements are performed and Γ_0 is the whole of the other boundaries.

Geosci. Instrum. Method. Data Syst. Discuss., doi:10.5194/gi-2016-32, 2016
Manuscript under review for journal Geosci. Instrum. Method. Data Syst.
Published: 1 November 2016

Geoscientific Instrumentation Methods and Data Systems Discussions

We denote with $L^2(\Omega)$ the space of square integrable functions on Ω and $H^1(\Omega)$ the Sobolev space

$$H^1(\Omega) = \{f \in L^2(\Omega)\} \text{ such as } \sum_{k=0}^{1} \int_{x\in\Omega} \left(\frac{\partial^k f}{\partial x^k}\right)^2 \mathrm{d}\Omega < \infty \tag{2}$$

The variational and Dirichlet formulations (Gartling, 2010) allows to write, on an orthogonal basis (ϕ_i) of $H^1(\Omega)$

$$\sum_i \left\{ \frac{\partial T_i}{\partial t} \int_\Omega \rho c \phi_i(x)\phi_j(x)\mathrm{d}\Omega + T_i \left[\int_{\partial\Omega} h\phi_i(x)\phi_j(x)\mathrm{d}\Gamma + \int_\Omega k\nabla\phi_i(x)\nabla\phi_j(x)\mathrm{d}\Omega \right] - \left[\int_{\partial\Omega} (\varphi\phi_j(x) + h\phi_j T_a)\,\mathrm{d}x \right] \right\} = 0 \ ,\forall j \tag{3}$$

For a numerical solution of the thermal problem, we consider a mesh of elements $\{\Omega^e\}$ and nodes $\{\mathcal{N}^e\}$. The approximation $T \approx \tilde{T}$ is made (Allaire, 2005), with $\tilde{T} \in V^q$ the discrete space of piecewise polynomials of degree $\leq q$ in each mesh element Ω^e

$$V^q = \{f \in H^1(\Omega) \text{ such as } f_{|\Omega^e} \in \mathbb{P}^q\} \tag{4}$$

with $\mathbb{P}^q$ the space of piecewise polynomials of degree $\leq q$. A basis of V^q is the piecewise polynomials (ϕ_i) of degree $\leq q$ such as

$$\phi_i(x_j) = \delta_{ij} \ , \forall x_j \in \mathcal{N}^e \tag{5}$$

where δ_{ij} is the Kronecker symbol.

The equation (3) is still valid for $\tilde{T}$ written in the basis of (ϕ_i). Therefore, to simplify the notation, T will refer to the approximated solution on the space V^q.

From the equation (3), we get a differential equation on time for the temperature at the nodes $\{T\}$

$$[M]\frac{\partial\{T\}}{\partial t} + [K]\{T\} = \{\Phi\} \tag{6}$$

This equation is temporally solved with an implicit Euler algorithm so the temperature is obtained at each node of the mesh and for each time step. Finally, in order to provide a more realistic modeling, white Gaussian noise is added to the (measured ?) computed temperature.

2.2 Thermal reconstruction

The aim of the inverse thermal problem is to get a reconstruction of the thermal capacity ρ_c and conductivity k in the investigated domain. To achieve this goal, we introduce a functional J to be minimized (Brouns, 2014) (Nassiopoulos and Bourquin,

Geosci. Instrum. Method. Data Syst. Discuss., doi:10.5194/gi-2016-32, 2016
Manuscript under review for journal Geosci. Instrum. Method. Data Syst.
Published: 1 November 2016

Geoscientific Instrumentation Methods and Data Systems Discussions
Open Access
EGU

2010). The minimization of this functional could be (or is ?) performed with the Levenberg-Marquardt algorithm. This algorithm needs the computation, at each iteration, of the gradient of the locally linearized functional, which is carried out with the adjoint state method. Note that, by using the adjoint state method, it is possible to get the adjoint equations which have a similar structure to thermal direct equations (1). The functional J is expressed as

$$J : u \mapsto \frac{1}{2}\|T(u) - T^m\|^2_{\mathcal{M}} + \frac{\varepsilon}{2}\|u - u^0\|^2_{\mathcal{R}} \tag{7}$$

with $u \in \mathcal{U}$ being the vector of thermal parameters $u = \{k, \rho c\}$ and $\mathcal{U}$ the space of unknowns:

$$\mathcal{U} = \left(L^\infty_+(\Omega)\right)^2 \text{ , } L^\infty_+(\Omega) = \{v \in L^\infty(\Omega), v \geq 0 \text{ a.e.}\} \tag{8}$$

In the above formula, $\theta(u)$ is the thermal state associated to u, ε is the Tikhonov parameter, u^0 is an *a priori* estimation of the thermal parameters u, θ^m are the measures obtained with the direct model at the location Γ_m for time scale $[0, t_a]$. Moreover, $\mathcal{M}$ is the space of measures $\mathcal{M} = L^2(\Gamma_m, L^2([0, t_a]))$. The norm in $\mathcal{M}$ is defined as (Brouns, 2014)

$$\|f\|^2_{\mathcal{M}} = \int_0^{t_a}\int_{\Gamma_m} f^2(x,t)\mathrm{d}\Gamma\mathrm{d}t \tag{9}$$

where $\mathcal{R} = \left(L^2(\Omega)\right)^2$ is the regularization space.

The inverse problem consists in finding $u \in \mathcal{U}$ such as:

$$u = \underset{v \in \mathcal{U}}{\arg\min} J(v) \tag{10}$$

To solve this non-linear optimization problem, we apply the Levenberg-Marquardt algorithm, which is frequently used to solve non-linear inverse problems, as thermal reconstruction (Jarny et al., 1991) or the reconstruction of electric conductivity (Bal et al., 2012). At each iteration, the Levenberg-Marquardt algorithm linearizes locally the functional in order to find a minimum point, which becomes the point around which the linearization occurs at the next iteration (Levenberg (1944)).

At each iteration, the functional J is linearized in $\tilde{J}_u$ next to the value of the reconstructed thermal parameters u at this iteration. For a small variation δu of the thermal parameters, it follows that

$$\tilde{J}_u(\delta u) = \frac{1}{2}\|T(u) + \delta T(u)\delta u - T^m\|^2_{\mathcal{M}} + \frac{\varepsilon}{2}\|u + \delta u - u^0\|^2_{\mathcal{R}} + \frac{\nu}{2}\|\delta u\|^2_{\mathcal{R}} \tag{11}$$

where ν is the damping parameter, which allows to define a confidence interval around u (Hanke, 2010).

The minimum of $\tilde{J}_u$ is reached in δu such as

$$\delta u = \underset{\delta v \in \mathcal{U}}{\arg\min} \tilde{J}_u(\delta v) \iff \tilde{J}'_u(\delta u) = 0 \tag{12}$$

Geosci. Instrum. Method. Data Syst. Discuss., doi:10.5194/gi-2016-32, 2016
Manuscript under review for journal Geosci. Instrum. Method. Data Syst.
Published: 1 November 2016

Geoscientific Instrumentation Methods and Data Systems Discussions
Open Access
EGU

where $\tilde{J}'_u$ is defined as

$$\tilde{J}_u(\delta u + \delta\tilde{u}) = \tilde{J}_u(\delta u) + \tilde{J}'_u(\delta u)\delta\tilde{u} + o(\|\delta\tilde{u}\|_{\mathcal{U}}) \tag{13}$$

To minimize $\tilde{J}_u$, we use the conjugate gradient method, which needs the computation of the differential $\tilde{J}'_u(\delta u)$.

The adjoint state method initially developed in the control theory (Lions (1971)) is also applied. Applying the adjoint method allows to keep the same equation structure and also to use the same resolution method for the direct and the inverse problem (Jarny et al., 1991; Brouns, 2014). Such method consists in introducing and computing the adjoint operator of $T'(u)$. First, we introduce $\delta\theta$, i.e. the solution of the tangent linear model (14)

$$\begin{cases} \rho c\frac{\partial\delta T}{\partial t} - \nabla\cdot(k\nabla\delta T) = \nabla\cdot(\delta k\nabla\theta) - \delta\rho c\frac{\partial T}{\partial t} & \text{for } (x,t)\in\Omega\times[0,t_a] \\ k\nabla\delta T\cdot\boldsymbol{n} = -\delta k\nabla T\cdot\boldsymbol{n} - (h+h_{ray})\delta T & \text{for } (x,t)\in\Gamma_m\times[0,t_a] \\ k\nabla\delta T\cdot\boldsymbol{n} = -\delta k\nabla T\cdot\boldsymbol{n} & \text{for } (x,t)\in\Gamma_0\times[0,t_a] \\ \delta T(x,0) = 0 & \text{for } x\in\Omega \end{cases} \tag{14}$$

Then, we introduce $\delta\theta^*$ i.e. the adjoint operator of $\delta\theta$. This operator is the solution of the adjoint problem (Jarny et al., 1991) (Brouns, 2014)

$$\begin{cases} -\rho c\frac{\partial\delta T^*}{\partial t} - \nabla\cdot(k\nabla\delta T^*) = 0 & \text{for } (x,t)\in\Omega\times[0,t_a] \\ k\nabla\delta T^*\cdot\boldsymbol{n} = -(h+h_{ray})\delta T^* + (T+\delta T - T^m) & \text{for } (x,t)\in\Gamma_m\times[0,t_a] \\ k\nabla\delta T^*\cdot\boldsymbol{n} = 0 & \text{for } (x,t)\in\Gamma_0\times[0,t_a] \\ \delta T^*(x,t_a) = 0 & \text{for } x\in\Omega \end{cases} \tag{15}$$

The adjoint model (15) has the same structure than the tangent linear model (14) and the direct model (1). Therefore, the adjoint and the tangent linear models can also be solved on the same mesh of the direct model with the same finite element formulation.

The differential of J_u can be computed with the optimal control theory by estimating (Brouns, 2014)

$$\begin{aligned} J'_u(\delta u)\delta\tilde{u} = &-\int_0^{t_a}\int_\Omega \delta\tilde{k}\nabla T\cdot\nabla\delta T^*\mathrm{d}\Omega\mathrm{d}t - \int_0^{t_a}\int_\Omega \delta\tilde{\rho c}\frac{\partial T}{\partial t}\delta T^*\mathrm{d}\Omega\mathrm{d}t \\ &+\varepsilon\int_\Omega \delta\tilde{k}\left(k+\delta k-k^0\right) + \delta\tilde{\rho c}\left(\rho c+\delta\rho c-\rho c^0\right)\mathrm{d}\Omega + \nu\int_\Omega \delta\tilde{k}\delta k + \delta\tilde{\rho c}\delta\rho c\mathrm{d}\Omega \end{aligned} \tag{16}$$

The conjugate gradient algorithm is applied at each iteration of the Levenberg-Marquardt algorithm. With $J'_u(\delta u)\delta\tilde{u}$, we can get a reconstruction of the thermal parameters k and ρ_c in the investigated domain.

Geosci. Instrum. Method. Data Syst. Discuss., doi:10.5194/gi-2016-32, 2016
Manuscript under review for journal Geosci. Instrum. Method. Data Syst.
Published: 1 November 2016

Geoscientific Instrumentation Methods and Data Systems Discussions
Open Access
EGU

3 Electromagnetic modeling

The GPR imaging of an unknown wall requires recording electric field measurements at the air-wall surface. The GPR is composed by a transmitting and a receiving antenna having a spatial common offset, which are moved simultaneously to gather data along a line. The transmitting antenna radiates an electromagnetic signal in the wall and a part of this signal is reflected by buried anomalies and detected by the receiving GPR antenna.

3.1 Electric field computation

For GPR signal modeling, we consider a 2D geometry consisting in a three-layered medium where the upper medium is free-space, the central medium is a lossy dielectric wall, and the lower medium is free-space (see fig.1). It is supposed that the upper air/wall interface is located at $z = 0$, having assumed an $x - z$ coordinate system with the x axis directed parallel to the air/wall surface and the z axis normal to it. The free-space is characterized by dielectric permittivity and magnetic permeability equal to ε_0 and μ_0. The wall has a relative dielectric permittivity equal to ε_b and an electrical conductivity equal to σ_b. All media are supposed to be non-magnetic (Soldovieri et al., 2007).

As well-known, the space-time behavior of the electromagnetic field in all mediums is governed by the Maxwell's equations (17) (Balanis, 2012)

$$\begin{cases} \nabla \wedge \boldsymbol{E} = -\frac{\partial \boldsymbol{B}}{\partial t} \\ \nabla \wedge \boldsymbol{B} = \frac{\partial \boldsymbol{D}}{\partial t} + \boldsymbol{J}_c + \boldsymbol{J}_s \\ \nabla \cdot \boldsymbol{D} = \rho \\ \nabla \cdot \boldsymbol{B} = \rho_m \end{cases} \tag{17}$$

where $\boldsymbol{E}$ is the electric field vector, $\boldsymbol{H}$ is the magnetic field vector, $\boldsymbol{J}_c$ is current density vector induced by the electric field, $\boldsymbol{J}_s$ is the impressed current density vector, $\boldsymbol{B}$ is the magnetic induction vector, $\boldsymbol{D}$ is the electric induction vector, ρ is the electric charge density and ρ_m is the magnetic charge density.

In isotropic media, $\boldsymbol{J}_c$, $\boldsymbol{B}$, and $\boldsymbol{D}$ are related to $\boldsymbol{E}$, and $\boldsymbol{H}$ by the constitutive laws (Balanis, 2012)

$$\begin{cases} \boldsymbol{J}_c = \sigma \boldsymbol{E} \\ \boldsymbol{D} = \varepsilon \boldsymbol{E} \\ \boldsymbol{B} = \mu \boldsymbol{H} \end{cases} \tag{18}$$

In order to get the electric field at the measurement points along the air/wall surface, the direct problem has to be solved based on the known geometrical and electromagnetic properties of the scenario. This problem is herein solved numerically by using the popular GprMax tool developed by Giannopoulos (Giannopoulos, 2005). The code discretizes Maxwell equations in space and time by means of the Finite Difference Time (FDTD) method based on the Yee's algorithm. The antennas are modeled

Geosci. Instrum. Method. Data Syst. Discuss., doi:10.5194/gi-2016-32, 2016
Manuscript under review for journal Geosci. Instrum. Method. Data Syst.
Published: 1 November 2016

Geoscientific Instrumentation Methods and Data Systems Discussions
Open Access
EGU

as electric line sources assumed invariant along the y-axis (Soldovieri et al., 2007). The perfectly matched layers (PMLs) are used to the terminate the computational domain in order to prevent spurious reflections of the electromagnetic waves from the outer boundaries. At each time step, the electric field measurements are recorded at the receiving antenna location. Moreover, a simulation is carried out for each position of the transmitting and receiving antennas in order to compute GPR data in the multi-bistatic configuration. Finally, in order to account for the effects of measurement noise, a white Gaussian noise is added to the computed electric field.

3.2 Electromagnetic inverse problem

The goal of GPR imaging is to reconstruct the dielectric properties of the investigated domain $\mathfrak{D}$ plane starting from the knowledge of the scattered field measurements taken at the surface of the structure under test.

Due to the linearity of Maxwell's equations (17), the electric field $\boldsymbol{E}$ at each measurement point can be decomposed into an incident and a scattered component. The first one $\boldsymbol{E}_{inc}$ is the electric field in absence of buried anomalies, while the second $\boldsymbol{E}_s$ is originated by the variation of subsurface dielectric properties with respect to background (Persico, 2014).

The scattering phenomenon can be conveniently described in terms of the electric contrast function χ (Persico and Bernini, 2005; Persico, 2014; Soldovieri et al., 2009):

$$\chi(x,z) = \frac{\varepsilon_{eq}(x,z) - \varepsilon_{eqb}}{\varepsilon_{eqb}} \tag{19}$$

where

$$\varepsilon_{eq}(x,z) = \varepsilon_0 \varepsilon_r(x,z) - j\frac{\sigma(x,z)}{2\pi f} \tag{20}$$

and

$$\varepsilon_{eqb} = \varepsilon_0 \varepsilon_b - j\frac{\sigma_b}{2\pi f} \tag{21}$$

are the equivalent complex dielectric permittivities of the target and the wall, respectively, and σ_b and ε_b are the conductivity and the relative dielectric permittivity of the wall.

The scattered electric field is related to the unknown contrast function χ by the integral equation (Persico, 2014)

$$E_s(x_s) = k_s^2 \int\int_{\mathfrak{D}} G_e(x_s, x', z') E(x_s, x', z') \chi(x', z') \mathrm{d}x' \mathrm{d}z' \tag{22}$$

where E_s is the scattered field datum probed at x_s, k_s is the wavenumber in the wall, G_e is the external Green's function, and E is the total field in D.

Geosci. Instrum. Method. Data Syst. Discuss., doi:10.5194/gi-2016-32, 2016
Manuscript under review for journal Geosci. Instrum. Method. Data Syst.
Published: 1 November 2016

Geoscientific Instrumentation Methods and Data Systems Discussions
Open Access
EGU

The electromagnetic inverse scattering problem is non-linear and ill-posed. This fact implies the necessity to apply a regularization scheme in order to obtain a stable solution. Furthermore, the non linear nature of the problem brings additional difficulties related to the avoidance of false solutions (local minima).

In order to avoid the non-linearity problem and reduce the computation complexity of the related data processing algorithms, the Born approximation is applied to linearize the problem and get a unique solution. According to Born approximation, strictly holding in the case of weakly scattering targets, the total field in D is approximated as the incident field, i.e. $E \approx E_{inc}$. Then, the scattering phenomenon is governed by the linear integral equation (22), (Leone and Soldovieri, 2003; Persico and Bernini, 2005; Soldovieri et al., 2007)

$$E_s(x_s) = k_s^2 \int\int_{\mathfrak{D}} G_e(x, x', z') E_{inc}(x_s, x', z') \chi(x', z') dx' dz' \tag{23}$$

In order to retrieve the unknown contrast function χ, the singular value decomposition (SVD) of the linear operator defined by the equation (23) is evaluated. Specifically, the singular system $\{\sigma_n, u_n, v_n\}$ is introduced with $\{\sigma_n\}$ being the sequence of singular values sorted in decreasing order, $\{u_n\}$ being the basis function in the unknown space, and $\{v_n\}$ being the basis functions in the data space. The regularization of the solution is achieved by means of the truncated SVD algorithm (Leone and Soldovieri, 2003; Persico and Bernini, 2005; Soldovieri et al., 2007).

$$\chi = \sum_{n=1}^{N} \frac{1}{\sigma_n} \langle E_s, v_n \rangle u_n \tag{24}$$

where $\langle , \rangle$ denotes the scalar product in the data space and N is a truncation index fixed usually fixed at the knee of the singular value curve in order to find a good compromise between accuracy and stability of the solution.

4 Coupling of thermal and electromagnetic methods

The GPR imaging method has some drawbacks. First of all, the retrieved contrast function depends on the electrical properties of the background (Soldovieri et al., 2011). Moreover, due to the application of the Born approximation, the reconstruction are only qualitative, i.e. they provide an indication about the position and approximate shape of the targets(Leone and Soldovieri, 2003; Persico and Bernini, 2005). It must be further stressed that some distortions unavoidably arise in GPR images due to multipath clutter (Gennarelli and Soldovieri, 2015).

The thermal reconstruction method also presents some drawbacks. The effusivity ratio has an important effect on the quality of the reconstructions (Crinière et al., 2014). The defect area can be overestimated for some kinds of inclusions. The reconstruction is also sensitive to the side effects (Brouns et al., 2014) and to the noise (Nassiopoulos and Bourquin, 2013).

In this work, we propose to reduce the area of the thermal investigation domain in order to mitigate the side effects and noise sensitivity if there is no inclusion close to the measurement points. This decrease of the investigation domain extent is performed when the GPR image indicates that there is no inclusion near the measurement points.

Geosci. Instrum. Method. Data Syst. Discuss., doi:10.5194/gi-2016-32, 2016
Manuscript under review for journal Geosci. Instrum. Method. Data Syst.
Published: 1 November 2016

Accordingly, we first perform a reconstruction of the wall with the GPR. This reconstruction allows defining a smaller investigation region where an inclusion is likely to be located. After, a thermal reconstruction is performed over this smaller domain.

To get a first location of the inclusions with the GPR, the spatial map defined by the normalized amplitude of the contrast function $\hat{\chi}$ is considered (Soldovieri et al., 2009)

$$\hat{\chi}(x,z) = \frac{|\chi(x,z)|}{\max\limits_{(x,z)\in \mathrm{D}} |\chi(x,z)|} \tag{25}$$

This function is null where the dielectric permittivity is equal to that of the background and different from zero over target regions. A threshold T_m is also introduced to get the characteristic function U_r (Soldovieri et al., 2009)

$$U_r(x,z) = \begin{cases} 1 & \text{if } \hat{\chi}(x,z) \geq T_m \\ 0 & \text{else} \end{cases} \tag{26}$$

which defines a binary image of the probed scene on the basis of the amplitude of the retrieved contrast function.

Based on the information retrieved from GPR images, we define three useful sub-domains for the thermal reconstruction (see figure 2).

The first sub-domain $\mathfrak{D}_1$ contains the elements of the thermal mesh located close to the points having a characteristic function equal to 1. This sub-domain is most likely to contain the discontinuities or inclusions detected with the GPR.

The second sub-domain $\mathfrak{D}_2$ contains the elements of the thermal mesh where the characteristic function is equal to 0; inclusions are supposed not to be located in this sub-domain.

To reduce the discontinuity between the two others sub-domains, we add a third sub-domain $\mathfrak{D}_3$ located between $\mathfrak{D}_1$ and $\mathfrak{D}_2$. This sub-domain aims at being an area in which an inclusion might be retrieved. $\mathfrak{D}_3$ is however different from $\mathfrak{D}_1$ insofar as the thermal reconstruction performed in this area takes into account the fact that the probability for an inclusion to be in this area is lower than in $\mathfrak{D}_1$.

Let us define $\mathcal{A}$ the set of points (x,z) such as $U_r(x,z) = 1$ and $\mathcal{B}$ the set of mesh element centroids used for the thermal reconstruction.

The sub-domain $\mathfrak{D}_1$ is made of the elements of centroid $(x,z) \in \mathcal{B}$ such as

$$\exists (x_0,z_0) \in \mathcal{A} \text{ such as } \begin{cases} |x - x_0| \leq l_{1x} \\ -l_{1z-} \leq z - z_0 \leq l_{1z+} \end{cases} \tag{27}$$

Geosci. Instrum. Method. Data Syst. Discuss., doi:10.5194/gi-2016-32, 2016
Manuscript under review for journal Geosci. Instrum. Method. Data Syst.
Published: 1 November 2016

Geoscientific Instrumentation Methods and Data Systems Discussions
Open Access
EGU

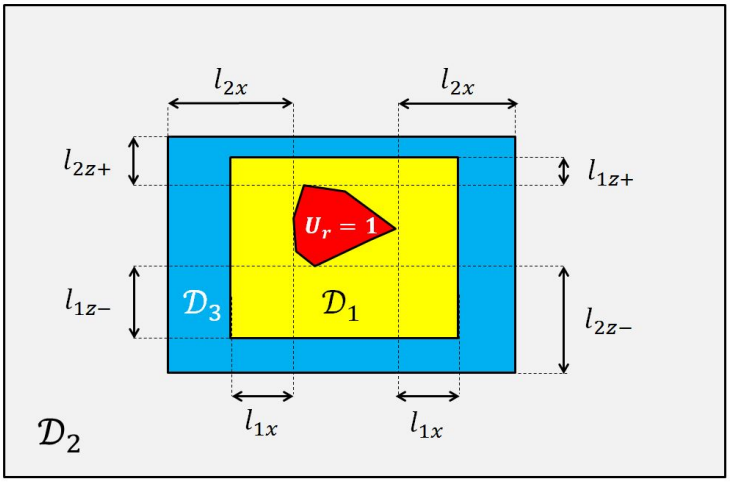

Figure 2. thermal sub-domains

The sub-domain $\mathfrak{D}_2$ is made of the elements of centroid $(x, z) \in \mathfrak{B}$ such as

$$\forall (x_0, z_0) \in \mathcal{A} \text{ such as } \begin{cases} |x - x_0| \geq l_{2x} \\ z_0 - z \geq l_{2z-} \text{ or } z - z_0 \geq l_{2z+} \end{cases} \tag{28}$$

Where l_{1x}, l_{2x}, l_{1z+}, l_{1z-}, l_{2z+} and l_{2z-} are length such as :

$$\begin{cases} l_{1x} \leq l_{2x} \\ l_{1z+} \leq l_{2z+} \\ l_{1z-} \leq l_{2z-} \end{cases} \tag{29}$$

The lower part of the inclusion can be badly located (Persico and Bernini, 2005). To take into account this effect, we add the following condition:

$$\begin{cases} l_{1z+} \leq l_{1z-} \\ l_{2z+} \leq l_{2z-} \end{cases} \tag{30}$$

The sub-domain $\mathfrak{D}_3$ is constituted of the elements of the thermal mesh which are not in $\mathfrak{D}_1$ neither in $\mathfrak{D}_2$.

The location of these sub-domains is shown in figure 2.

Geosci. Instrum. Method. Data Syst. Discuss., doi:10.5194/gi-2016-32, 2016
Manuscript under review for journal Geosci. Instrum. Method. Data Syst.
Published: 1 November 2016

Geoscientific Instrumentation Methods and Data Systems Discussions
Open Access
EGU

In the case $\mathfrak{D}_3 \neq \varnothing$, we define on $\mathfrak{D}_3$ the norm $\|\cdot\|_{\mathfrak{D}_3}$ relative to the scalar product $\langle\cdot,\cdot\rangle_{\mathfrak{D}_3}$ defined such as

$$\langle a,b\rangle_{\mathfrak{D}_3} = \int_{\mathfrak{D}_3} a(x)b(x)\mathrm{d}\Omega \tag{31}$$

We propose to take into account the *a priori* information coming from the electromagnetic characteristic function U_r by the following way (see Fig.3).

The sub-domain $\mathfrak{D}_2$ is far from the *a priori* location of inclusions or discontinuities. The assumption is made that no defect is located in $\mathfrak{D}_2$. Consequently, we suppose that there is no inclusion in this sub-domain and that the thermal properties u in this sub-domain are those of the background u^0.

$$\forall x \in \mathfrak{D}_2, u(x) = u^0(x) \tag{32}$$

To take into account the fact that the sub-domain $\mathfrak{D}_3$ is located between $\mathfrak{D}_1$, where the inclusions have been reconstructed with the GPR reconstruction, and $\mathfrak{D}_2$, where we have made the assumption that there is no inclusion, we suppose that for sub-domain $\mathfrak{D}_3$ the thermal properties are close to those of the background. Anyway, we let the option that thermal parameters could not be equal to the background parameters in order to be able to reveal a potential inclusion which would have been located wrong or not identified with the GPR. To do that, we add to the functional J a constraint term :

$$\frac{\mu}{2}\|u-u^0\|^2_{\mathfrak{D}_3} \tag{33}$$

Where μ is a scalar allowing to adjust the intensity of the constraint.

We define $\mathcal{U}'$ the subspace of $\mathcal{U}$ such as $\forall (x,z) \in \mathfrak{D}_2, u(x,z) = u^0(x,z)$

The optimization problem becomes: find $u \in \mathcal{U}'$ such as

$$u = \underset{v\in\mathfrak{U}'}{\arg\min} J(v) \tag{34}$$

where

$$J(u) = \frac{1}{2}\|T(u)-T^m\|^2_{\mathcal{M}} + \frac{\varepsilon}{2}\|u-u^0\|^2_{\mathcal{R}} + + \frac{\mu}{2}\|u-u^0\|^2_{\mathcal{D}_3} \tag{35}$$

To minimize J, the differential $J'_u(\delta u)\delta\tilde{u}$, introduced in section 2.2 needs to be evaluated. This differential has been evaluated, without constraint term, in equation (16) and becomes

Geosci. Instrum. Method. Data Syst. Discuss., doi:10.5194/gi-2016-32, 2016
Manuscript under review for journal Geosci. Instrum. Method. Data Syst.
Published: 1 November 2016

Geoscientific Instrumentation Methods and Data Systems Discussions

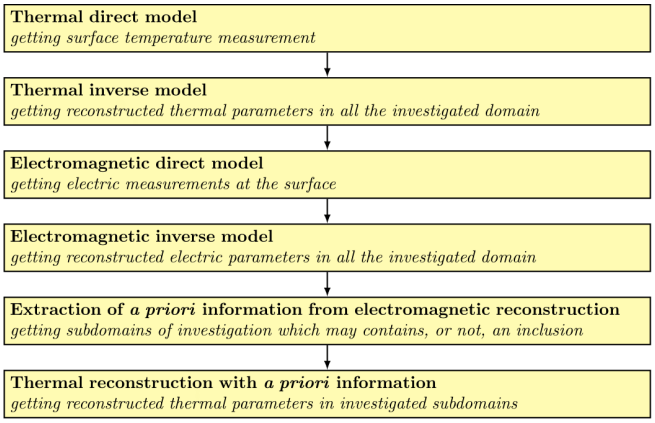

Figure 3. Joint thermal and electromagnetic imaging approach.

Table 1. Thermal and electric properties of the materials

material	ρc [J · K^{-1} · m^{-3}]	k [W · m^{-1} · K^{-1}]	ε_r	σ [S · m^{-1}]
limestone	2420×855	2.22	8	0.01
wood	600×1900	0.15	5	10^{-8}

$$J'_u(\delta u)\delta\tilde{u} = -\int_0^{t_a}\int_\Omega \delta\tilde{k}\nabla T\cdot\nabla\delta T^*\mathrm{d}\Omega\mathrm{d}t - \int_0^{t_a}\int_\Omega \delta\tilde{\rho c}\frac{\partial T}{\partial t}\delta T^*\mathrm{d}\Omega\mathrm{d}t + \varepsilon\int_\Omega \delta\tilde{k}\left(k+\delta k-k^0\right)+\delta\tilde{\rho c}\left(\rho c+\delta\rho c-\rho c^0\right)\mathrm{d}\Omega$$
$$+\nu\int_{\mathfrak{D}_3}\delta\tilde{k}\left(k+\delta k-k^0\right)+\delta\tilde{\rho c}\left(\rho c+\delta\rho c-\rho c^0\right)\mathrm{d}\Omega+\nu\int_\Omega \delta\tilde{k}\delta k+\delta\tilde{\rho c}\delta\rho c\mathrm{d}\Omega \tag{36}$$

This new formulation of the functional J has to be compared to the first one (16) expressed in section 2.2, as it integrates now a new constraint term. This term will allow us to exploit a priori information retrieved from GPR data inversion.

5 Numerical tests

The numerical examples reported in this study is concerned with a limestone wall containing a wood inclusion (see fig.4). The electric and thermal properties of these materials can be found in the pertinent literature 1, (Dumoulin et al., 2010) (Giannopoulos, 2005) and are listed in Tab.1. The wall has a length of 2m, a height of 1.5m, and the wood inclusion is 1m long and 10cm thick. The top of this inclusion is located at depth of 40cm.

Geosci. Instrum. Method. Data Syst. Discuss., doi:10.5194/gi-2016-32, 2016
Manuscript under review for journal Geosci. Instrum. Method. Data Syst.
Published: 1 November 2016

Geoscientific Instrumentation Methods and Data Systems Discussions
Open Access
EGU

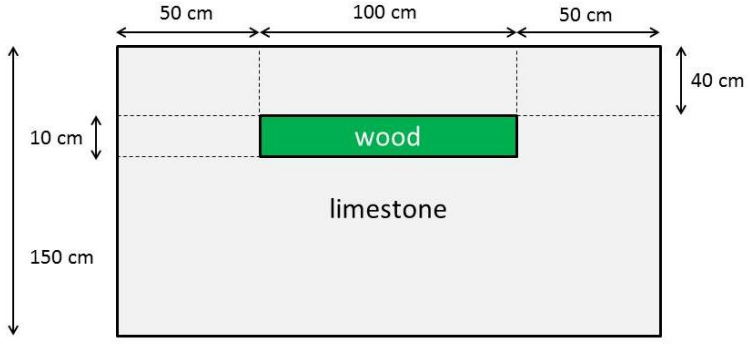

Figure 4. Geometry of the simulated scenario

Table 2. Lengths used to generate the three sub-domains

parameter	l_{1x}	l_{1z+}	l_{1z-}	l_x	l_{1z+}	l_{1z-}
length [m]	0.1	0.05	0.8	0.1	0.05	0.8

The synthtetic GPR data are computed thanks to GPRMax code, by considering a Ricker pulse radiated at the central frequency of 1300MHz. The data are gathered along the observation line ranging from $x = 0.1m$ to $x = 1.9m$ with a step of 3cm.

The investigation domain for GPR reconstruction has the same size of the wall and it is discretized with a step of 1.4cm in both directions. For the GPR recosntruction, we exploit a frequency band [100,2600] MHz, which is discretized with a step equal to 30MHz.

The TSVD algorithm is applied with a threshold on the singular values equal to -30dB, i.e. the singular values larger than 0.0316 times the maximum singular value are retained.

Then, to get the three investigation sub-domains, we use the parameters summarized in tab.2

As regards with the thermal direct model, we define the following synthetic periodic thermal loading at the monitored surface Γ_m

$$\begin{cases} T_a(t) = 12 + 5\sin(\omega t - \phi) \\ T_s(t) = -5 + 12\sin(\omega t - \phi) \\ \Phi_{rad}(t) = 250 \times \frac{1}{2}\left(\sin(\omega t - \phi) + |\sin(\omega t - \phi)|\right) \end{cases} \tag{37}$$

where T_a and T_s are expressed in $^\circ$C and Φ_{rad} in $\mathrm{W \cdot m^{-2}}$. The measurements are collected over a time interval of five days. The convective exchange coefficient is equal to $h = 10\ \mathrm{Wm^{-2}K^{-1}}$. The equivalent radiative exchange coefficient is evaluated

Geosci. Instrum. Method. Data Syst. Discuss., doi:10.5194/gi-2016-32, 2016
Manuscript under review for journal Geosci. Instrum. Method. Data Syst.
Published: 1 November 2016

Geoscientific Instrumentation Methods and Data Systems Discussions
Open Access
EGU

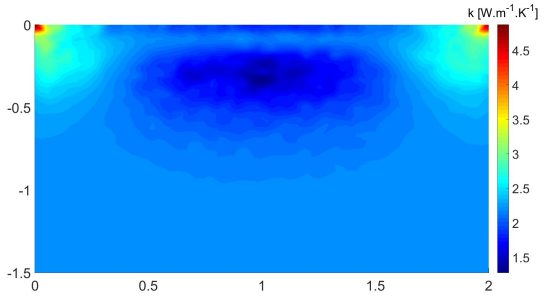

Figure 5a. Reconstructed conductivity

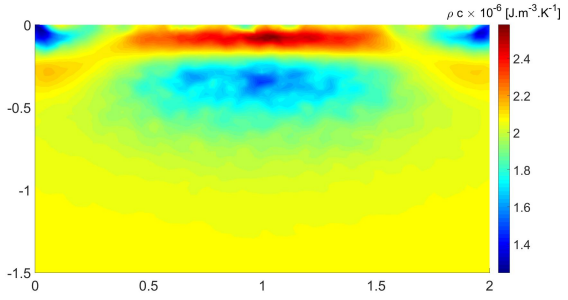

Figure 5b. Reconstructed capacity

as $h_{rad} = \sigma\varepsilon\left(T_{surf} + T_s\right)\left(T_{surf}^2 + T_s^2\right)$, where T_{surf} is equal mean air temperature and T_s to the mean of sky temperature. A white Gaussian noise with an amplitude equal to $0.5°$C is added to the data calculated in accordance with the direct model.

The reconstructed fields for thermal parameters without *a priori* information (not geometry information inferred by GPR inversion) are shown in figures 5a and 5b, respectively.

In order to analyze these images in a simple but quantitative way, we implement the following approach to identify the contour shape of the reconstructed anomaly. To this end, we analyze both the values of the reconstructed thermal parameters and their gradients. An element of the mesh is part of a contour if both reconstructed values, k and ρc, are distant by at least a % of the background parameters. This criterion aims at excluding from the inclusion all the elements having reconstructed parameters close to the background parameters. The threshold $a = 10\%$ is chosen for this study.

We suppose that the thermal parameters have a strong variability along the contour of the inclusion and assume that, at the contours of the inclusion, the gradient norms of both reconstructed parameters are higher than elsewhere in the investigated domain. On the basis of this consideration, we assume that a point (x, z) belongs to the contour of an inclusion only if

$$\begin{cases} \frac{\|\nabla k(x,z)\|}{k^0(x,z)} \geq b \\ \frac{\|\nabla \rho c(x,z)\|}{\rho c^0(x,z)} \geq b \end{cases} \tag{38}$$

After processing, closed contours that verified the above condition (38) are kept and their interior constitute a set of sub-domains that belongs to defective area. At that stage, no filtering on the size of defective area is applied, to preserve multiple detection possibilities.

In order to have a first estimation of the contours, we initiate the threshold b to 0 and select the points of the investigated domain satisfying both criteria. After, we increase the value of b until significant variations in the size or the number of the reconstructed inclusions occur. Beyond this critical value b_0, we observe that at least one main contour which exists with $b < b_0$ is not closed yet. Here, we have empirically chosen a threshold $b = 0.5$. (this sentence is not clear)

With both criteria, we get the reconstruction of the inclusion without *a priori* information shown in figure 6.

Geosci. Instrum. Method. Data Syst. Discuss., doi:10.5194/gi-2016-32, 2016
Manuscript under review for journal Geosci. Instrum. Method. Data Syst.
Published: 1 November 2016

Geoscientific Instrumentation Methods and Data Systems Discussions
Open Access
EGU

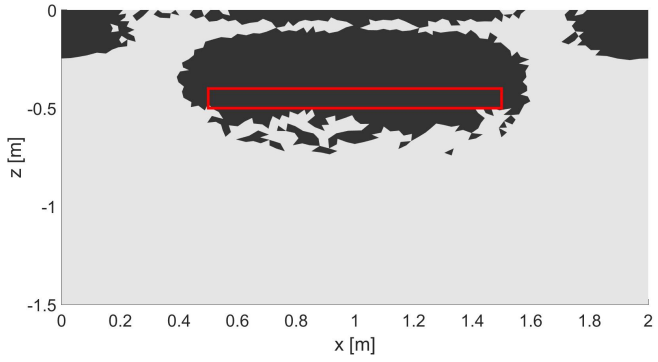

Figure 6. Reconstruction of inclusion with thermal method without *a priori* information

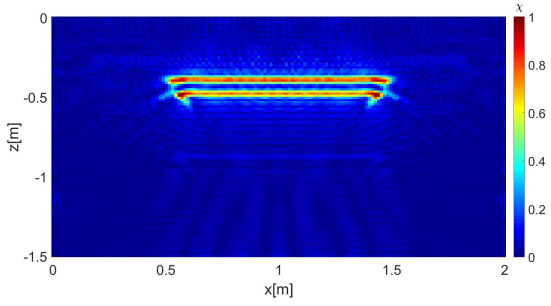

Figure 7a. Reconstructed contrast function **(caption checked too)**

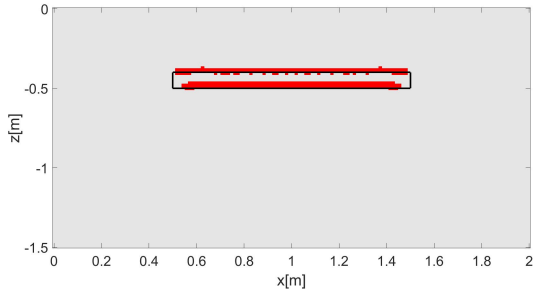

Figure 7b. Reconstructed characteristic function

Let us turn to consider the case if the thermal reconstruction when the information about the geometry is gained by GPR reconstruction. The reconstructed (normalized) contrast function is shown in figure 7a and the corresponding geometry of the inclusion is highlighted by the characteristic function in fig. 7b.

The deduced thermal sub-domains are shown in figure 8. The thermal reconstruction applied on the sub-domains $\mathfrak{D}_1$, $\mathfrak{D}_2$ and $\mathfrak{D}_3$ lead to the thermal fields presented on figures 9a for the conductivity and 9b for the capacity.

The reconstruction of the inclusion is shown on figure 10, in this case we have empirically chosen a gradient threshold $b = 2.2$.

To complete our study, we focus on the case the inclusion is constituted of air or steel instead of wood. The air is characterised by a relative dielectric permittivity equal to 1, eheras the steel can be assumed as a perfectly electrical conducting object. The thermal properties of these materials are described in table 4, (Dumoulin et al., 2010; Giannopoulos, 2005).

As can be observed, the location and the shape of the inclusion are better identified with *a priori* information. The area of the reconstructed inclusion is lower with *a priori* information and closer than the area of the initial inclusion, regardless the nature of the inclusion.

Geosci. Instrum. Method. Data Syst. Discuss., doi:10.5194/gi-2016-32, 2016
Manuscript under review for journal Geosci. Instrum. Method. Data Syst.
Published: 1 November 2016

Geoscientific Instrumentation Methods and Data Systems Discussions
Open Access
EGU

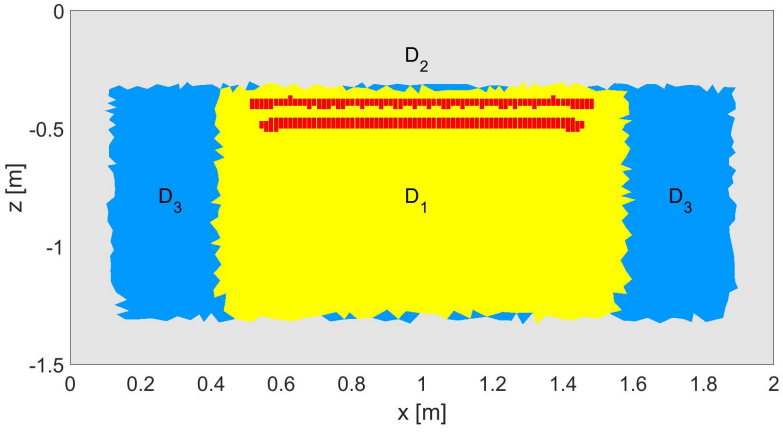

Figure 8. Reconstruction of inclusions with thermal method without *a priori* information

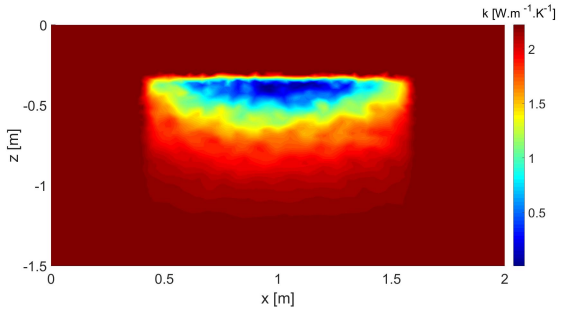

Figure 9a. Reconstructed conductivity with *a priori* information

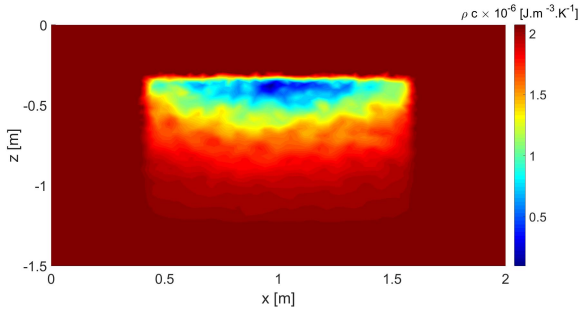

Figure 9b. Reconstructed capacity with *a priori* information

In practice, we focus the minimization of the functional J on two sub-domains when we have *a priori* information. These two sub-domains do not include here the part of the initial investigated domain located close to the surface, so the side effects are highly reduced with the GPR information. In particular, the variations of the thermal parameters close to the surface, visible on figures 5a and 5b do not interfere if we use *a priori* information. In fact, with the GPR reconstruction, we get the information that there is no inclusion close to the surface, so there is no research of inclusion next to the surface. The noise added to thermal measurements have quite no effect on the reconstruction because the high-frequency of this noise cannot propagate far from the surface effect (the thermal diffusion from surface act as a low pass filter). The coupling of these two methods allows to highly reduce the side effects and to get an improvement of the shape of the reconstructed inclusion.

However, we can notice that the reconstructed thermal properties (thermal conductivity and heat capacity) values encompass the location of the inclusion, but also connected areas in the non affected part of the material matrix. The relative differences between the reconstructions and the targets are reported in table 4. The relative errors for the heat capacity are significantly improved by using the joint approach excepted for inclusion filled with air. The relative errors for the thermal conductivity

Geosci. Instrum. Method. Data Syst. Discuss., doi:10.5194/gi-2016-32, 2016
Manuscript under review for journal Geosci. Instrum. Method. Data Syst.
Published: 1 November 2016

Geoscientific Instrumentation Methods and Data Systems Discussions
Open Access
EGU

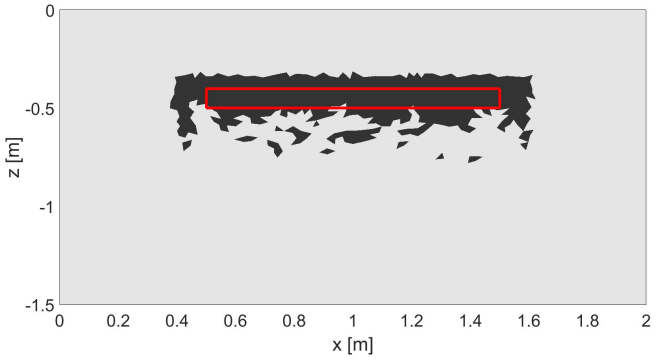

Figure 10. Reconstruction of inclusions with thermal method with *a priori* information

Table 3. Thermal and electric properties of the materials

material	$\rho c\ [\mathrm{J \cdot K^{-1} \cdot m^{-3}}]$	$k\ [\mathrm{W \cdot m^{-1} \cdot K^{-1}}]$	ε_r	$\sigma\ [\mathrm{S \cdot m^{-1}}]$
air	1.225×1006	0.0242	1	0
steel	8055×480	15.1	1	1.11×10^6

remain important, but care must be taken while making that analysis as the inclusion nature have low thermal conductivity excepted for steel. For instance, air thermal conductivity is very low and small numerical error will affect significantly the relative error. Nonetheless, the reconstructed parameters are coherent : the reconstructed values are higher than those of the background for steel, and lower for wood and air, as it was expected. Finally, the inclusion shape reconstruction is enhanced, though this reconstruction phase could take benefit of more advanced post-processing approaches. In particular, we want to

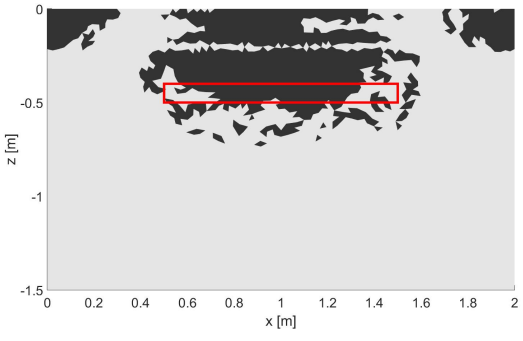

Figure 11a. Reconstructed inclusion of air without *a priori* information

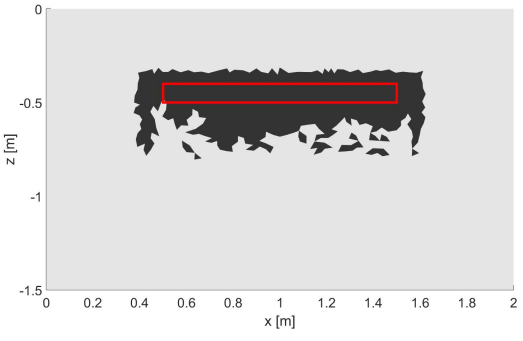

Figure 11b. Reconstructed inclusion of air with *a priori* information

Geosci. Instrum. Method. Data Syst. Discuss., doi:10.5194/gi-2016-32, 2016
Manuscript under review for journal Geosci. Instrum. Method. Data Syst.
Published: 1 November 2016

Geoscientific Instrumentation Methods and Data Systems Discussions
Open Access
EGU

Table 4. Properties of the reconstructed inclusions

material	$\overline{\rho c}$	ρc	error(ρc)	$\overline{k}$	k	error(k)	S	S (target)	error(S)
wood (no GPR)	1.89×10^6	1.14×10^6	66 %	2.00	0.15	1233 %	0.63	0.10	530 %
wood (GPR)	1.05×10^6	1.14×10^6	-7.9 %	1.00	0.15	566 %	0.30	0.10	200 %
air (no GPR)	1.83×10^6	1.23×10^3	1.5×10^5 %	1.78	0.0242	7255 %	0.46	0.10	360 %
air (GPR)	7.59×10^5	1.23×10^3	6.2×10^4 %	0.820	0.0242	3288 %	0.41	0.10	310 %
steel (no GPR)	2.24×10^6	3.87×10^6	-42 %	2.40	15.1	-84 %	0.71	0.10	610 %
steel (GPR)	2.94×10^6	3.87×10^6	-24 %	2.87	15.1	-81 %	0.29	0.10	190 %

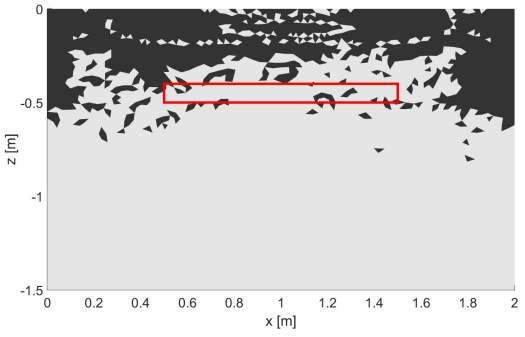

Figure 12a. Reconstructed inclusion of steel without *a priori* information

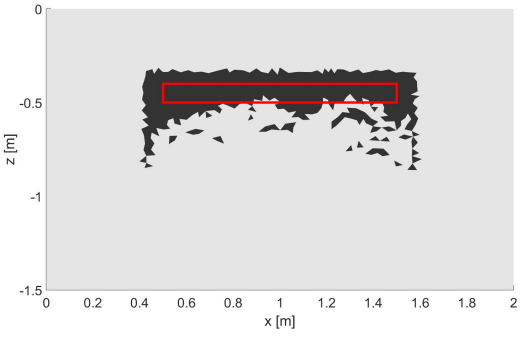

Figure 12b. Reconstructed inclusion of steel with *a priori* information

point out results obtained for the steel inclusion for which it can be observed that the joint thermal and electromagnetic approach allows us now to better reconstruct the inclusion and not only detect it by signal processing approach.

6 Conclusions

In this numerical study, we have proposed a diagnostic approach for thick wall structures combining thermal and GPR imaging approaches in order to improve the fidelity of the reconstruction results obtained with only one method.

The thermal method is based on the minimization of a functional, which is achieved with the Levenberg-Marquardt algorithm by computing a gradient with the adjoint state method.

The GPR imaging problem has been formulated by resorting to a linearized inverse scattering model based on the Born approximation. The resulting linear problem has been inverted via the truncated singular value decomposition scheme.

The combination of both reconstruction methods has been then presented. Based on GPR reconstruction, three sub-domains have been identified. The first one is the most likely to contain inclusions, the second one is far from potential inclusions

Geosci. Instrum. Method. Data Syst. Discuss., doi:10.5194/gi-2016-32, 2016
Manuscript under review for journal Geosci. Instrum. Method. Data Syst.
Published: 1 November 2016

revealed by the GPR. The third one is located among the previous ones. A constraint term has been added to the functional to minimize in order to take into account the a-priori information provided by GPR images.

Numerical examples have been reported and confirmed improved performance in terms of location of the inclusion, shape of the inclusion, area, and thermal parameters. However, the thermal conductivity is still far from the true inclusion conductivity.

The future research work will focus on the validation of the proposed approach against experimental data on a dedicated test site in outdoor conditions.

Geosci. Instrum. Method. Data Syst. Discuss., doi:10.5194/gi-2016-32, 2016
Manuscript under review for journal Geosci. Instrum. Method. Data Syst.
Published: 1 November 2016

Geoscientific Instrumentation Methods and Data Systems Discussions
Open Access
EGU

References

Allaire, G.: Analyse numerique et optimisation : Une introduction à la modelisation mathematique et à la simulation numerique, École Polytechnique, 2005.

Alperovich, L., Eppelbaum, L., Zheludev, V., Dumoulin, J., Soldovieri, F., Proto, M., Bavusi, M., and Loperte, A.: A new combined wavelet methodology applied to GPR and ERT data in the Montagnole experiment (French Alps), Journal of Geophysics and Engineering, 10, 2013.

Bal, G., Naetar, W., Scherzer, O., and Schotland, J.: The Levenberg–Marquardt iteration for numerical inversion of the power density operator, J. Inverse Ill-Posed Probl., 21, 265–280, 2012.

Balanis, C. A.: Advanced Engineering Electromagnetics (Second Edition), John Wiley and Sons, 2012.

Beck J.V., Blackwell B., S. C.: Inverse heat conduction: ill-posed problems, Wiley, 1985.

Brouns, J.: Développement d'outils numériques pour l'audit énergétique des bâtiments, Ph.D. thesis, Université Paris-Est, École doctorale SIE, 2014.

Brouns, J., Crinière, A., Dumoulin, J., Nassiopoulos, A., and Bourquin, F.: Diagnostic de structures de génie civil : Identification des propriétés spatiales et de la surface d'un défaut, 2014.

Crinière, A., Dumoulin, J., Ibarra-Castanedo, C., and Maldague, X.: Inverse model for defect characterisation of externally glued CFRP on reinforced concrete structures: comparative study of square pulsed and pulsed thermography, Quantitative InfraRed Thermography, 11, 84–114, 2014.

Daniels, D. J.: Ground Penetrating Radar, Institution of Engineering and Technology, 2nd edition edn., 2004.

Dumoulin, J. and Boucher, V.: Infrared thermography system for transport infrastructures survey with inline local atmospheric parameter measurements and offline model for radiation attenuation evaluations, Journal of Applied Remote Sensing, 8, 084 978–1 to 19, 2014.

Dumoulin, J., Ibos, L., Ibarra-Castanedo, C., Mazioud, A., Marchetti, M., Maldague, X., and Bendada, A.: Active infrared thermography applied to defect detection and characterization on asphalt pavement samples: comparison between experiments and numerical simulations, Journal of Modern Optics, 57, 1759–1769, 2010.

Dumoulin, J., Crinière, L., and Averty, R.: Detection and thermal characterization of the inner structure of the "Musmeci" bridge deck by infrared thermography monitoring, Journal of Geophysics and Engineering, 10, 64 003–64 013, 2013.

Eppelbaum, L.: Geophysical observations at archaeological sites: Estimating informational content, Archaeological Prospection, 21, 25–38, 2014.

Gartling, D.K; Reddy, J. N.: The Finite Element Method in Heat Transfer and Fluid Dynamics, Third Edition, CRC series in computational mechanics and applied analysis, CRC Press, 3rd ed edn., 2010.

Gennarelli, G. and Soldovieri, F.: Multipath Ghosts in Radar Imaging: Physical Insight and Mitigation Strategies, IEEE Journal of Selected Topics in Applied Earth Observations and Remote Sensing, 8, 1078–1086, 2015.

Giannopoulos, A.: Modelling ground penetrating radar by GprMax, Construction and Building Materials, 19, 755–762, 2005.

Hanke, M.: The regularizing Levenberg-Marquardt scheme is of optimal order, Journal of integral equations and applications, 22, 259–283, 2010.

Jarny, Y., Osizik, M. N., and Bardon, J. P.: A general optimization method using adjoint equation for solving multidimensional inverse heat equation, Int. J. Heat Mass Transfer, 34, 2911–2919, 1991.

Leone, G. and Soldovieri, F.: Analysis of the distorted Born approximation for subsurface reconstruction: truncation and uncertainties effects, IEEE Transactions on geoscience and remote sensing, 41, 66–74, 2003.

Levenberg, K.: A method for the solution of sertains problems to least squares, Applied mathematics, 2, 164–168, 1944.

Lions, J. L.: Optimal Control of Systems Governed by Partial Differential Equations, Grundlehren Der Mathematishen Wissenschaften 170, Springer, 1971.

Nassiopoulos, A.: Identification rapide de la température dans les structures de génie civil, Ph.D. thesis, École des Ponts ParisTech, 2008.

Nassiopoulos, A. and Bourquin, F.: Fast three-dimensional temperature reconstruction, Comput. Methods Appl. Mech. Engrg., 199, 3169–3178, 2010.

Nassiopoulos, A. and Bourquin, F.: On-site building walls characterization, Numerical Heat Transfer, Part A, 63, 179–200, 2013.

Ozisik, M. N.: Inverse heat transfer: fundamentals and applications, Taylor & Francis, 1 edn., 2000.

Persico, R.: Introduction to Ground Penetrating Radar: Inverse Scattering and Data Processing, IEEE Press Series on Electromagnetic Wave Theory, Wiley-IEEE Press, 1 edn., 2014.

Persico, R. and Bernini, R.: The role of the measurement configuration in inverse scattering from buried objects under the Born approximation, IEEE Transactions on antennas and propagation, 53, 1875–1887, 2005.

Soldovieri, F., Hugenschmidt, J., Persico, R., and Leone, G.: A linear inverse scattering algorithm for realistic GPR applications, New Surface Geophysics, 5, 29–41, 2007.

Soldovieri, F., Prisco, G., and Persico, R.: A strategy for the determination of the dielectric permittivity of a lossy soil exploiting GPR surface measurements and a cooperative target, Journal of Applied Geophysics, 67, 288–295, 2009.

Soldovieri, F., Solimene, R., Lo Monte, L., Bavusi, M., and Loperte, A.: Sparse reconstruction from GPR data with applications to radar detection, IEEE Transactions on instrumentation and measurement, 60, 1070–1079, 2011.